STSM 2

TESTING OF A NEW LIGHTWEIGHT RADAR SYSTEM FOR TOMOGRAPHICAL RECONSTRUCTION OF CIRCULAR STRUCTURES

VISITING SCIENTIST: ALESSANDRO FEDELI, UNIVERSITY OF GENOA, GENOA, ITALY
ALESSANDRO.FEDELI@EDU.UNIGE.IT

HOST SCIENTISTS: JANA JE□OVÁ & SÉBASTIEN LAMBOT, UNIVERSITÉ CATHOLIQUE DE LOUVAIN, LOUVAIN-LA-NEUVE, BELGIUM
JANA.JEZOVA@UCLOUVAIN.BE & SEBASTIEN.LAMBOT@UCLOUVAIN.BE

STSM DATES: 12ND SEPTEMBER – 23RD SEPTEMBER 2016

1. PURPOSE OF THE STSM

Ground penetrating radar (GPR) is becoming one of the most effective tools for geophysical inspection and evaluation. Many different areas of application exist: from the conventional task of buried object detection in subsurface regions to the recent developments related to the assessment of tree trunks [1, 2] or other civil engineering structures [3].

On one hand, the need of devising new and more efficient GPR measurement systems has a key importance, because the emerging applications often require portable and lightweight – but powerful – systems. In particular, an accurate modelling of the physical effects that occur between the antenna structure and the soil interface is fundamental for a correct acquisition and interpretation of GPR measurements.

On the other hand, there is an ever-growing interest in the development of advanced data processing techniques for GPR, since the raw data are usually very difficult to interpret and skilled

professionals are often required for deducing the actual configuration of the buried objects. In particular, both qualitative and quantitative imaging algorithms developed in the area of electromagnetic inverse scattering theory [4] may be successfully applicable to the processing of GPR data. The benefits of applying such techniques reside in the possibility of retrieving not only the shape and location of the hidden objects or inclusions, but also the distribution of their electromagnetic properties.

At the intersection point between these two emerging research trends, the main goal of the present STSM was the combination of the experimental and modelling skills of the Georadar Research Centre at the Université Catholique de Louvain (UCL), Belgium, with the data processing techniques developed at the Applied Electromagnetics Laboratory of the DITEN Department of the University of Genoa (UNIGE), Italy.

Therefore, the STSM has been focused on both: the acquisition and the inversion of experimental measurements. Such experimental data were obtained by using a novel radar prototype. Circular structures in free space and buried in a sandy soil were considered. The new system was tested in several different configurations and with different antennas. The acquired experimental data were pre-processed with a state-of-the-art calibration technique developed at UCL. Furthermore, the possibility of applying advanced inversion methods aimed at reconstructing the characteristics of the inspected targets both qualitatively and quantitatively was explored with promising results.

2. DESCRIPTION OF THE WORK CARRIED OUT DURING THE STSM

In this STSM, two different kinds of work were done: experimental measurements and data processing. The experimental activities were carried out at the laboratory of the Georadar Research Centre of the Université Catholique de Louvain in Louvain-la-Neuve,

Belgium. The experimental test site includes a 3D high-precision positioning system, two sand boxes of different size, a circular cylinder filled with sand, a large copper sheet for antenna calibration, and a vector network analyser, which is used for acquiring measurements. After the GPR data acquisition, MATLAB and C++ codes were utilized for the processing steps.

2.1. TEST OF THE RADAR PROTOTYPE WITH DIFFERENT ANTENNAS

Several types of GPR custom antennas were tested during the STSM for being used with the new radar prototype. All the antennas were calibrated by fitting the accurate far-field model developed by Lambot et al. [5].

In particular, the calibration was performed by measuring the complex reflection coefficient of the antennas at different distances from a large square copper sheet with 3 m side length (Figure 1). Both air- and dielectric-coupled antennas were calibrated, as reported in Table 1.

FIG. 1 – Antenna placed at some distance from a large copper sheet for the calibration phase.

TABLE 1– Antennas tested and calibrated during the STSM.

ANTENNA	TYPE	CALIBRATED FREQUENCY RANGE
#1	Aluminum air coupled	800 MHz – 4 GHz
#2	Copper air coupled	800 MHz – 4 GHz
#3	Dielectric coupled	800 MHz – 4 GHz

2.2. ANTENNA COUPLING WITH SAND OF DIFFERENT VOLUMETRIC WATER CONTENT

Some experiments aimed at verifying the coupling of different kinds of antennas in front of a sand box with different levels of sand moisture were done (Figure 2).

FIG. 2 – Measurements in small sand box with different volumetric water contents.

Antennas #1, #2 and #3 were used for this task, acquiring for each antenna four A-scans at different distances from the interface with the sand layer. As sketched in Figure 3, the sand box has a square

section with side length $s = 0.96$ m, its height is $h = 0.1$ m and it is contained in a wood structure made of four laths $t = 0.02$ m thick. At the bottom, a conducting square metal plate of $l = 1$ m side length is positioned.

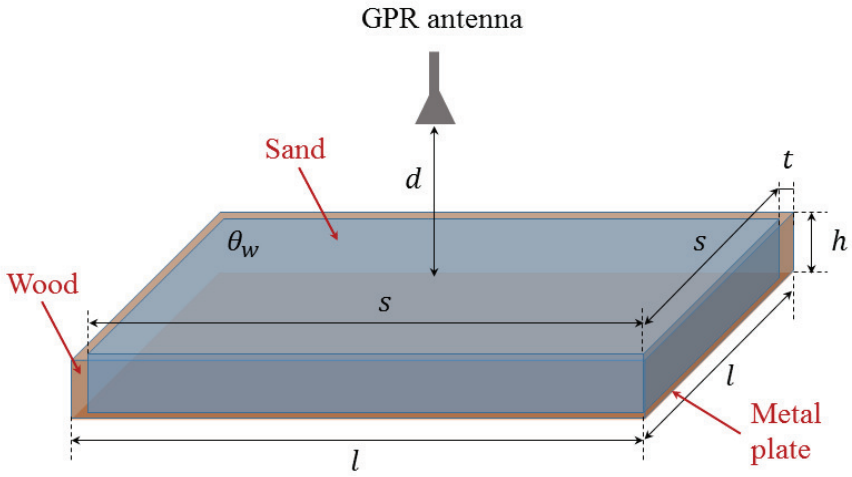

FIG. 3 – Geometrical configuration of the sand box used for the A-scan measurements with different levels of volumetric water content and different antennas.

The antennas under test were placed, in turn, at the center of the sand box at a distance d from the air-sand interface. The considered distances are $d = \{0, 1, 10, 20\}$ cm. Specific quantities of water were added to the sand and accurately mixed with it in order to obtain values of soil percentage volumetric water content $\theta_w = \{0, 3, 6, 9, 12, 16, 20, 24\}$ %. After having moistened and carefully mixed the sand, A-scans with the three custom antennas were measured for each considered value of distance d.

2.3 MEASUREMENTS IN SAND BOX WITH BURIED OBJECTS

The second experimental work carried out during this STSM concerns the acquisition of B-scans in a sand box (Figure 4) with different antennas and several values of distance between the

antenna and the soil interface. The box is a parallelepiped with horizontal sides of length $s = 3\,\mathrm{m}$ and height $h = 1\,\mathrm{m}$, and it is filled with dry sand. At the bottom, a $3\,\mathrm{m}\times3\,\mathrm{m}$ metal plate is placed. Two different test sets were prepared.

FIG. 4 – An empty PVC circular cylinder is being buried during the preparation of the test sets for the B-scans in the sand container.

In the first one, whose cross section is schematized in Figure 5, a circular metallic rebar of length $l_1 = 2.5\,\mathrm{m}$ and diameter $d_1 = 0.03\,\mathrm{m}$ is located at the centre of the box, $z_1 = 0.1\,\mathrm{m}$ deep. In addition, an empty PVC tube with length $l_2 = 0.9\,\mathrm{m}$, outer diameter $d_2 = 0.08\,\mathrm{m}$ and thickness $t_2 = 0.0018\,\mathrm{m}$ was positioned at a depth $z_2 = 0.085\,\mathrm{m}$. The surface of the sand was levelled by using a tool mounted on the arm of the 3D positioning system. It is worth noting that three other water-filled pipes are present in the sand box from a previous experiment.

However, we have positioned the new targets such as their scattering contributions in the B-scan remained separate. By using antenna #1, B-scans of length $L = 2.4\,\mathrm{m}$ were taken, at distances $d = \{0.01, 0.1, 0.15, 0.2, 0.3\}\,\mathrm{m}$ above the soil. With antenna #3, we have acquired B-scans of length $L = 2.1\,\mathrm{m}$ at distances $d = \{0.01, 0.12, 0.2\}\,\mathrm{m}$. In all cases, a constant spacing step of $1\,\mathrm{cm}$ between measurements was used.

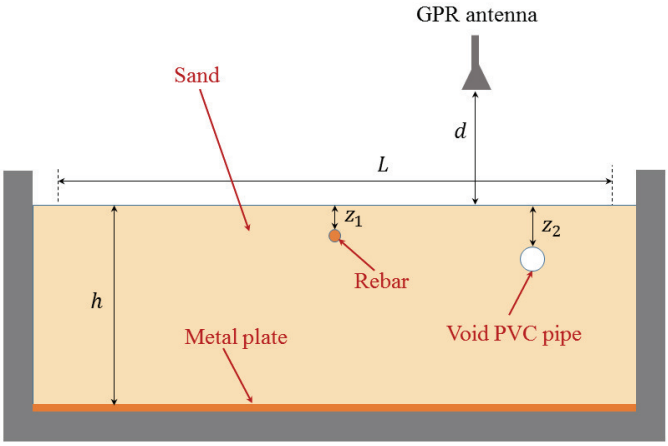

FIG. 5 – First test set. Configuration of the sand box with one buried void PVC pipe and a metallic rebar.

The second test set that was prepared in the sand box (Figure 6) includes three pipes of different sizes and filling materials. Two of them (cylinder #1 and cylinder #3) were filled with air.

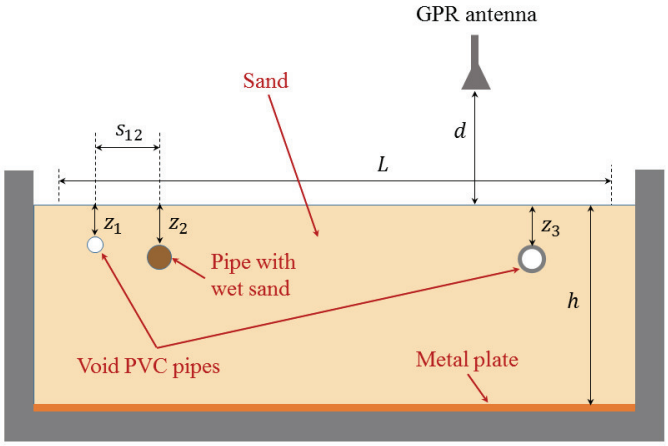

FIG. 6 – Second test set. Configuration of the sand box with two buried void PVC pipes of different sizes and one PVC tube filled with wet sand of 24% volumetric water content.

The other cylinder (cylinder #2) was completely filled with wet sand characterized by $\theta_w = 24\%$ volumetric water content (see Figures 7 and 8).

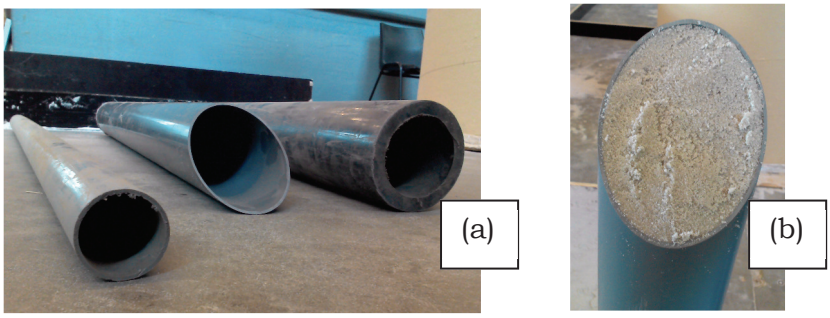

FIG. 7 – Second test set. PVC circular cylinders before being buried in the sand box: (a) all the cylinders empty; (b) cylinder #2 filled with wet sand with 24% volumetric water content.

FIG. 8 – Second test set. PVC circular cylinders during burial: (a) cylinders #1 and #2; (b) cylinder #3.

The main parameters of the buried targets involved in this experiment are summarized in Table 2. The reported values of depth are referred to the top of the cylinders, and were measured after the sand levelling. The horizontal spacing between cylinder #1 and cylinder #2 is $s_{12} = 0.185$ m (referred to the centre of the pipes). B-scans of length $L = 2.4$ m (subdivided into 241 equally spaced steps with 1 cm distance between each other) were taken,

with antenna #1 located at a distances $d = \{0.01, 0.1, 0.2\}$ m above the soil.

TABLE 2 – Properties of the tubes buried in the sand box for the second test set.

CYLINDER	FILLING MATERIAL	LENGTH	OUTER DIAMETER	THICKNESS	TOP DEPTH
#1	Air	1.16 m	0.04 m	0.0018 m	0.125 m
#2	Wet sand	0.90 m	0.08 m	0.0018 m	0.155 m
#3	Air	1.03 m	0.09 m	0.0120 m	0.130 m

2.4 MEASUREMENTS AROUND CIRCULAR CYLINDER WITH VOID INCLUSION

The last set of measurements was taken around a circular cylinder with one void inclusion (Figure 9).

FIG. 9 – Measurements around the circular cylinder with void inclusion.

The geometrical configuration of the analysed structure is shown in Figure 10. The outer structure is a paper cylinder with outer diameter $d_o = 0.82$ m. Inside, there is a void PVC tube with diameter $d_i = 0.4$ m. The internal space between the two cylinders is filled by dry sand. The GPR measurements were acquired starting from the initial position indicated in Figure 10 and with counter clockwise rotation direction. The angular spacing between two subsequent measurement points was chosen equal to $\Delta\phi = 5.6°$. Antennas #1 and #2 were used for inspecting this structure, with distances $d = \{0, 0.01, 0.1, 0.2\}$ m between the antenna aperture and the outer paper cylinder. The angular spacing was kept the same in all cases.

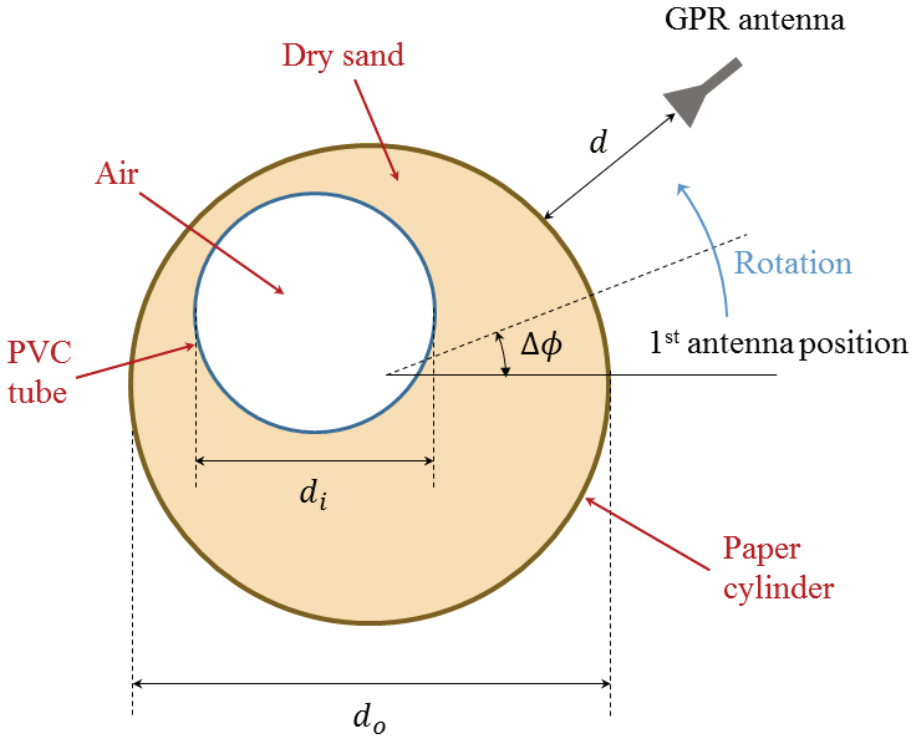

FIG. 10 – Geometrical configuration of the experiments concerning one circular cylinder with void inclusion.

2.5 RECONSTRUCTION METHODS APPLIED TO GPR DATA

After the acquisition of GPR measurements, the pre-processing method proposed in [5] was applied for filtering out antenna effects. To this end, the calibration described above was employed for each antenna. Subsequently, some of the measured GPR data were further processed with two reconstruction methods developed at the Applied Electromagnetics Laboratory of the University of Genoa and modified during the STSM in order to be applied to the present cases.

The first method that was used with experimental data is the qualitative reconstruction procedure outlined in [6]. Essentially, it is based on a filtering step combined with a Delay-and-Sum beamforming. First of all, the field scattered by the buried objects is estimated and separated from the scattering contributions of the soil. After that, a qualitative image of the subsurface domain is obtained by properly combining all the measured data through a time-shift and an integral operator. From the resulting image, the location of the buried targets can be estimated, and rough information about their shape is provided.

The second technique used for processing the experimental data is a quantitative inexact-Newton inverse scattering method [7]. The goal of this procedure is to retrieve the spatial distribution of the dielectric properties (i.e., dielectric permittivity and electric conductivity) in the investigation region. The algorithm, which is able to simultaneously process data acquired at different frequencies, is composed by two nested iterative loops. Since the electromagnetic inverse scattering problem without approximations is nonlinear [8], the outer loop performs a linearization of the scattering equation around the current estimated dielectric properties by means of a Gauss-Newton algorithm. Furthermore, an inner Landweber method solves the obtained linear problem in a regularized way. This method has been extensively tested in presence of simulated data. During the

STSM, the experimental validation of the method has been initiated.

3. Description of the main results obtained during the STSM

In this section, the most significant results obtained in the framework of the present STSM are presented. It is worth remarking that the results shown here are still preliminary, but really promising. The joint work started with this STSM is currently in progress. In particular, the implementation of some modifications in the processing method is being studied, in order to improve the obtained results.

3.1 Experiments with sand of different volumetric moisture content

For an effective application of data processing algorithms and models, the performance of the GPR antenna used for acquiring measurements represents a crucial point. In particular, on one hand the antenna should be well-coupled with the material that surrounds the targets to be inspected. On the other hand, the bandwidth should be sufficiently large in order to collect information about the target in a wide range of frequencies. Both these important parameters have been analyzed for several antennas with different structures during the STSM.

As described in Section 2, A-scans were recorded with the antennas placed on a sand box with different volumetric water contents. Antennas #1, #2, and #3 were used, in the frequency range between 800 MHz and 3 GHz. The results are shown in Figures 11, 12, 13.

Antenna #1 gives the best results. When the volumetric water content is low, a lighter reflection arises from the air-sand interface, and the reflection from the bottom conducting plate is more evident. An opposite trend occurs in presence of high levels

of volumetric water content. The results obtained with antenna #2 are still good, but less stable. Because of the restricted bandwidth, the calibration is more critical, and the signal-to-noise ratio is reduced. Worse results were obtained with antenna #3. Even when the antenna is in contact with the inspected structure, it is difficult to see the reflections from the bottom metal plate. A-scans appear to be significantly corrupted by noise at greater distances from the soil level, too.

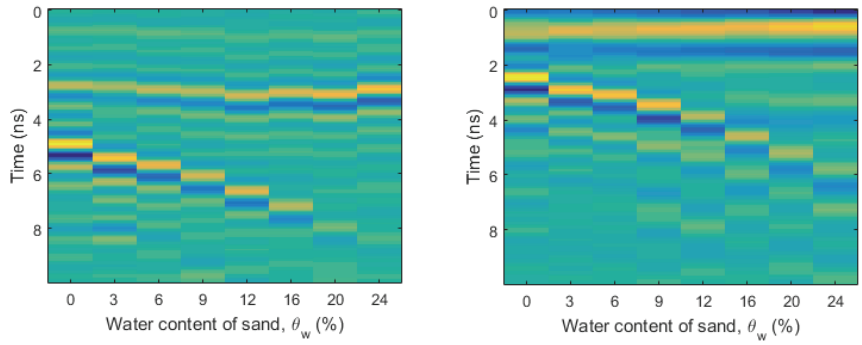

FIG. 11 – A-scans acquired on the sand box with antenna #1, versus the volumetric water content of sand, for different distances from the soil d: $d = 0$ m in the left panel; $d = 0.2$ m in the right panel.

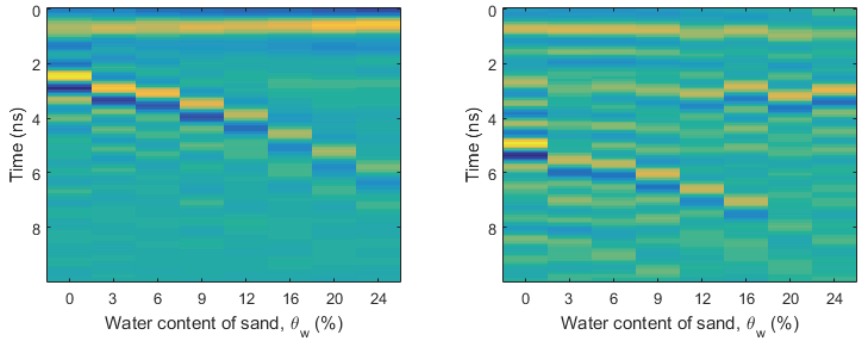

FIG. 12 – Same as in Fig. 11, with Antenna #2.

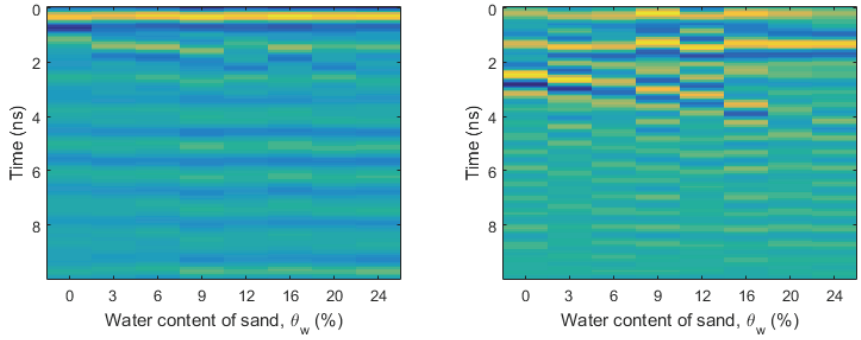

FIG. 13 – Same as in Fig. 11, with Antenna #3.

3.2 SAND BOX WITH BURIED OBJECTS

Some B-scan measurements acquired during the STSM are reported in this section. Let us consider the first test set. In Figure 14, the raw data of the B-scan with antenna #1 at distance $d = 0.01$ m above the soil is depicted. Frequencies between 800 MHz and 3 GHz were considered.

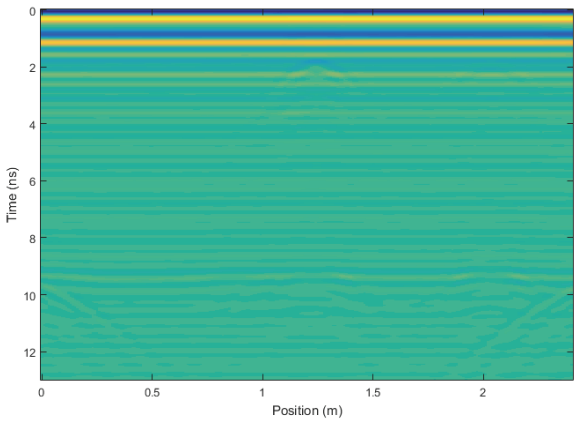

FIG. 14 – First test set in sand box. B-scan acquired with antenna #1 at a distance $d = 0.01$ m from the soil level. No filters to remove antenna effects are applied.

The pre-processed data, obtained after the application of the filter to remove antenna effects are reported in Figure 15. Clearly, this step is fundamental in order to see the reflection hyperbolas arising from the buried objects, that otherwise are hidden behind the internal reflections inside the antenna structure. Since this pre-processing step utilizes the far field model, a better filtering can be made when the antenna is more distant from the soil level. Close to the soil, the near field model described in [9] should be used.

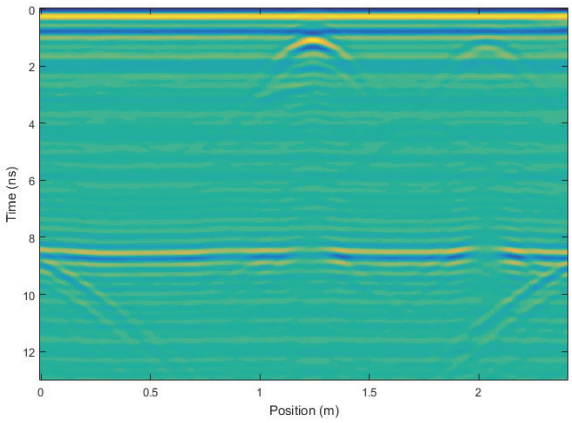

FIG. 15 – First test set in sand box. B-scan acquired with antenna #1 at a distance $d = 0.01$ m from the soil level. Antenna filters are applied.

As an example, in Figures 16 and 17 the raw and the pre-processed B-scans with the same antenna at a distance $d = 0.15$ m from the soil interface are shown. It is easy to see that the filtering step based on the far field model is performing better in this case.

Similar remarks still hold for the results obtained with antenna #3. However, this antenna has a restricted bandwidth. Therefore, only frequencies in the range between 800 MHz and 1.7 GHz were considered.

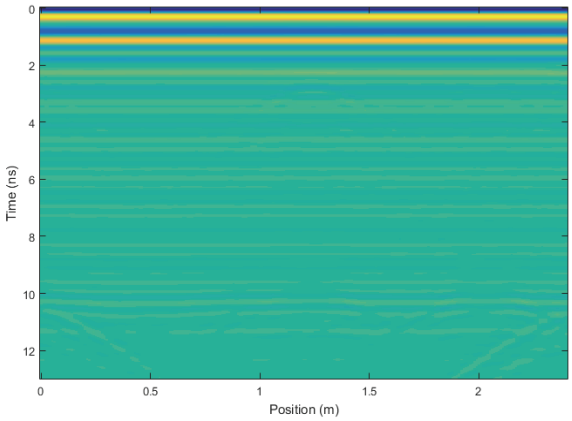

FIG. 16 – First test set in sand box. B-scan acquired with antenna #1 at a distance $d = 0.15$ m from the soil level. No filters to remove antenna effects are applied.

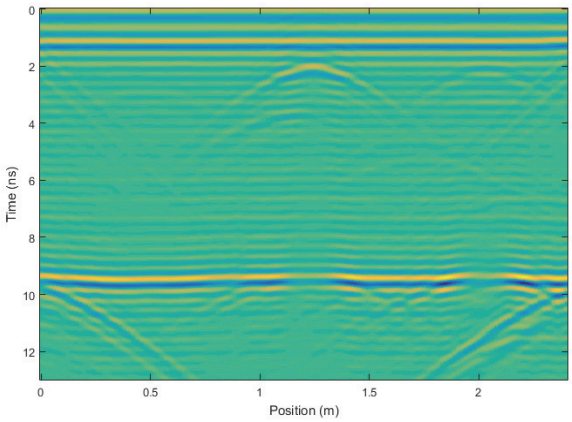

FIG. 17 – First test set in sand box. B-scan acquired with antenna #1 at a distance $d = 0.15$ m from the soil level. Antenna filters are applied.

In Figures 18 and 19 the raw and pre-processed results with antenna #3 placed $d = 0.01$ m far from the soil are presented. Not all the antenna effects are removed in this case, and buried objects are barely visible.

With an increased distance from the soil (e.g. when $d = 0.12$ m, as reported in Figures 20 and 21) results are better and antenna effects are removed. However, the limited bandwidth influences the resolution of the B-scan image significantly.

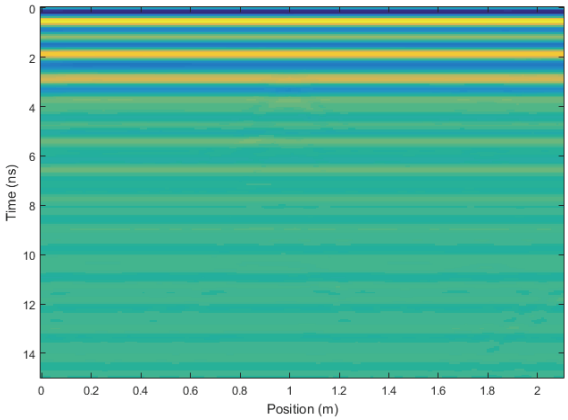

FIG. 18 – First test set in sand box. B-scan acquired with antenna #3 at a distance $d = 0.01$ m from the soil level. No filters to remove antenna effects are applied.

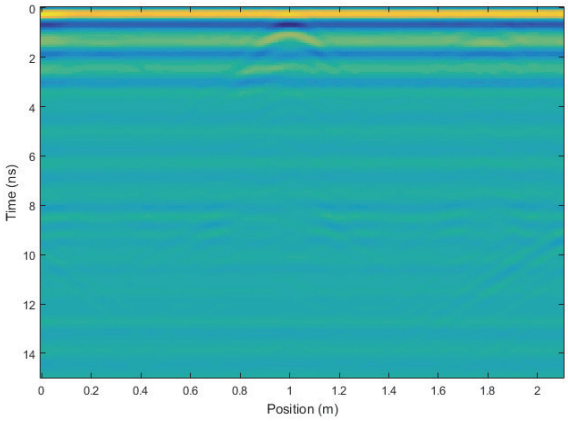

FIG. 19 – First test set in sand box. B-scan acquired with antenna #3 at a distance $d = 0.01$ m from the soil level. Antenna filters are applied.

For the second test set, B-scans collected at heights $d = 0.01$ m and $d = 0.1$ m by using Antenna #1 are shown in Figures 22 – 25. Raw data are in Figures 22 and 24, the processed ones are in Figures 23 and 25. The filtering step appears to be very important and it works better when the far field condition is fulfilled.

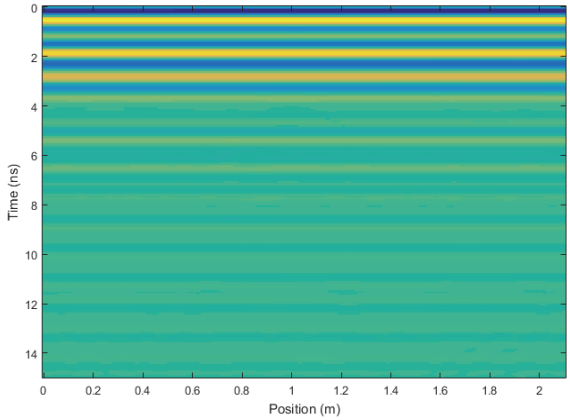

FIG. 20 – First test set in sand box. B-scan acquired with antenna #3 at a distance $d = 0.12$ m from the soil level. No filters to remove antenna effects are applied.

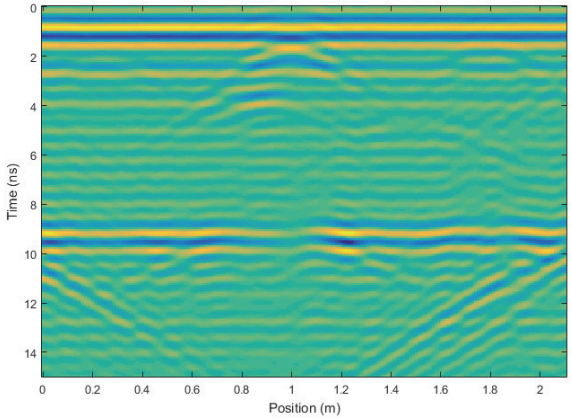

FIG. 21 – First test set in sand box. B-scan acquired with antenna #3 at a distance $d = 0.12$ m from the soil level. Antenna filters are applied.

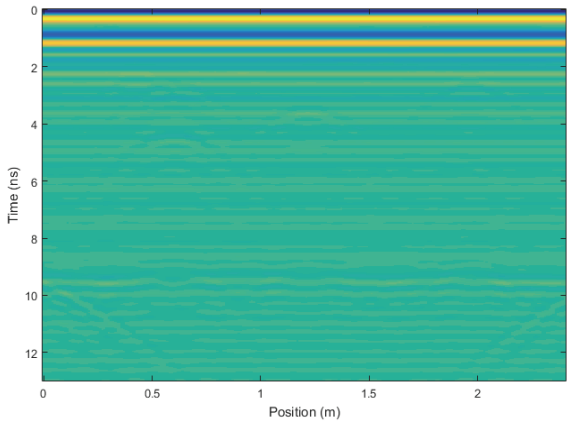

FIG. 22 – Second test set in sand box. B-scan acquired with antenna #1 at a distance $d = 0.01$ m from the soil level. No filters to remove antenna effects are applied.

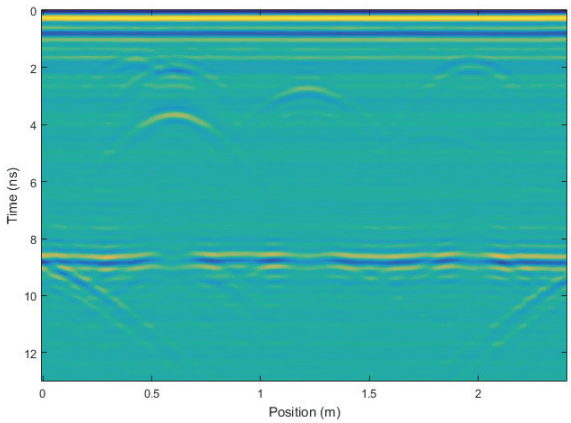

FIG. 23 – Second test set in sand box. B-scan acquired with antenna #1 at a distance $d = 0.01$ m from the soil level. Antenna filters are applied.

Reconstructions results of the targets belonging to the first test set in sand box are shown in Figure 26. Here, the qualitative imaging algorithm presented above was applied to the B-scan at $d = 0.01$ m. As it can be seen, the targets were detected in all cases.

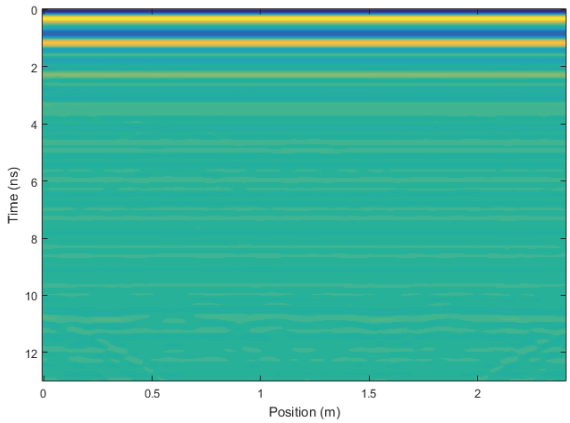

FIG. 24 – Second test set in sand box. B-scan acquired with antenna #1 at a distance $d = 0.1$ m from the soil level. No filters to remove antenna effects are applied.

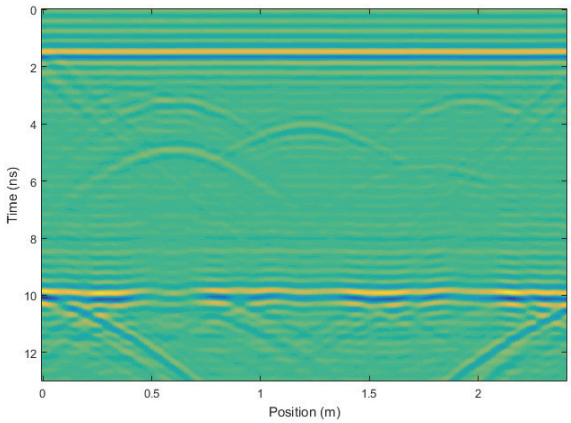

FIG. 25 – Second test set in sand box. B-scan acquired with antenna #1 at a distance $d = 0.1$ m from the soil level. Antenna filters are applied.

A preliminary quantitative reconstruction of the buried void PVC tube is shown in Figure 27. The tube is correctly identified as filled by air (relative dielectric permittivity $\varepsilon_r = 1$). Further developments

will be devoted to the detailed analysis of the quantitative imaging results.

Qualitative reconstructions of the second test set are reported in Figure 28, by using the B-Scan at a distance $d = 0.01$ m from the soil. All the three buried cylinders were detected. However, the reconstruction of cylinder #1 is partially obscured by the very close cylinder #2, which has a significantly stronger contrast with respect to the background dielectric properties.

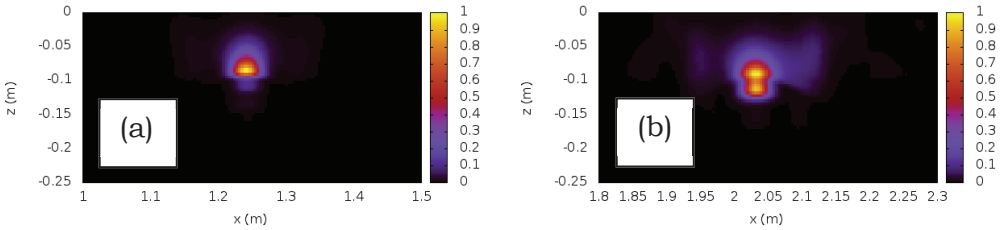

FIG. 26 – First test set in sand box. Qualitative reconstruction results obtained with antenna #1 at a distance $d = 0.01$ m from the soil level: (a) metallic rebar; (b) void PVC tube.

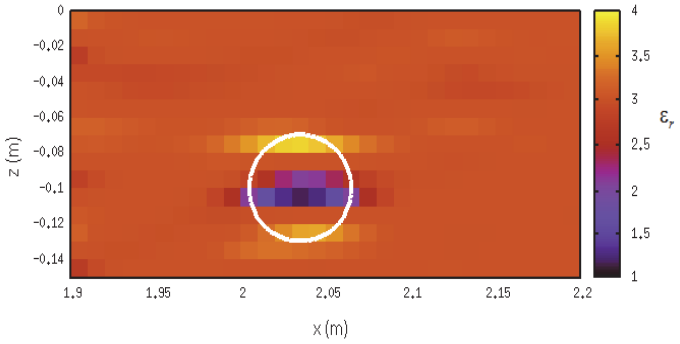

FIG. 27 – Reconstructed distribution of the relative dielectric permittivity obtained with antenna #1 at a distance $d = 0.20$ m from the soil level.

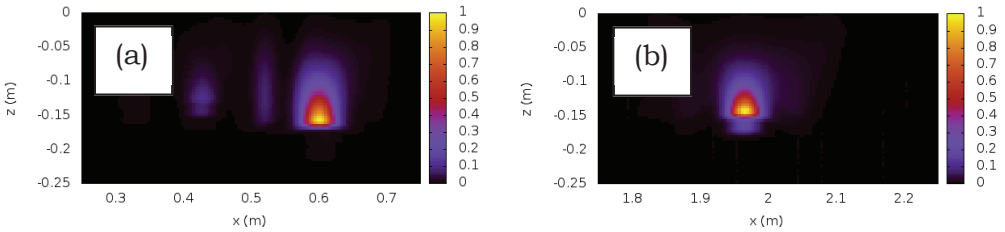

FIG. 28 – Second test set in sand box. Qualitative reconstruction results obtained with antenna #1 at a distance $d = 0.01$ m from the soil level: (a) cylinder #1 and cylinder #2; (b) cylinder #3.

3.3 CIRCULAR CYLINDER WITH VOID INCLUSION

The filtered B-scans acquired with antenna #1 and antenna #2 at two different distances from the circular structure described above are reported in Figures 29 – 32. Results with antenna #1 (Figure 29 and 31) are more stable. The sinusoidal feature due to the inner void cylinder is clearly visible in all cases.

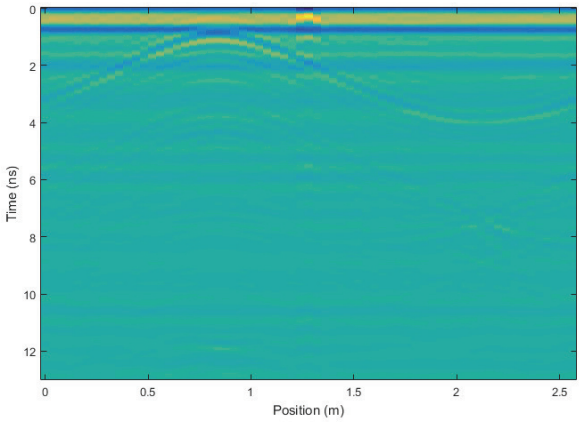

FIG. 29 – Circular cylinder with void inclusion. B-scan acquired with antenna #1 at a distance $d = 0$ m from the sample. Antenna filters are applied.

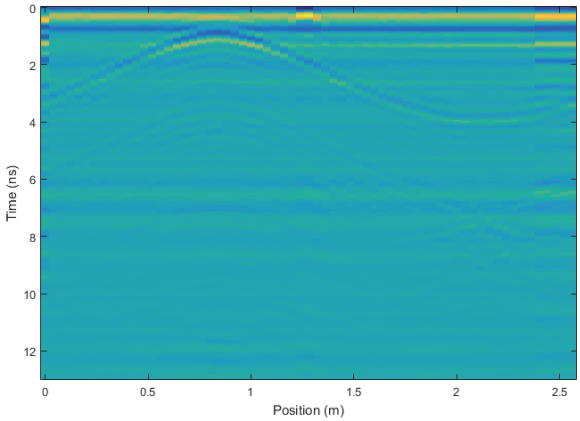

FIG. 30 – Circular cylinder with void inclusion. B-scan acquired with antenna #2 at a distance $d = 0$ m from the sample. Antenna filters are applied.

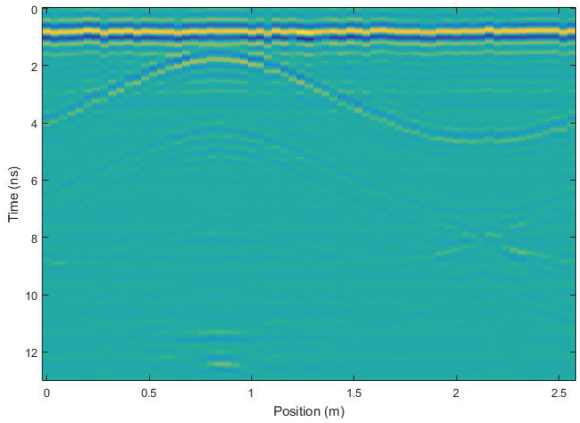

FIG. 31 – Circular cylinder with void inclusion. B-scan acquired with antenna #1 at a distance $d = 0.1$ m from the sample. Antenna filters are applied.

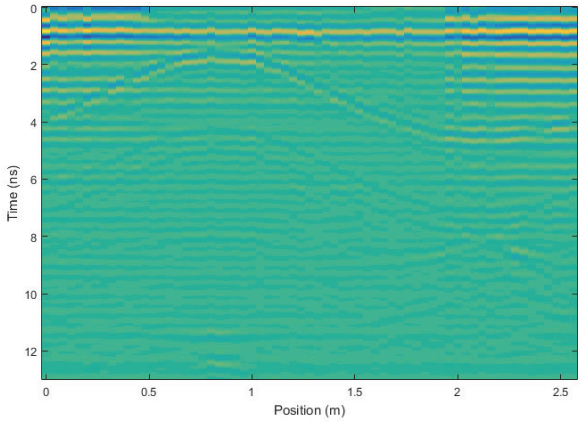

FIG. 32 – Circular cylinder with void inclusion. B-scan acquired with antenna #2 at a distance $d = 0.1$ m from the sample. Antenna filters are applied.

In Figures 33 and 34, the results obtained by means of the qualitative reconstruction method applied to the circular cylinder configuration are shown.

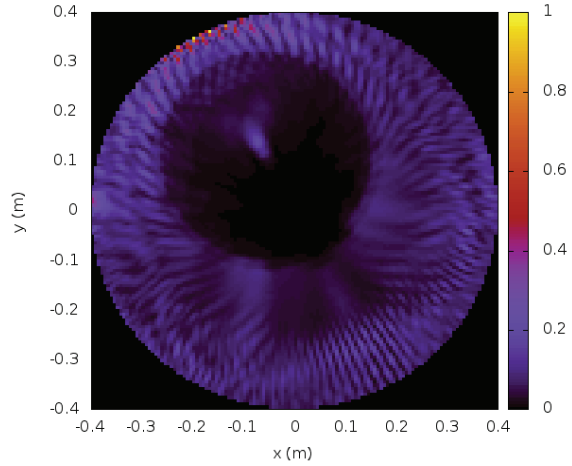

FIG. 33 – Circular cylinder with void inclusion. Qualitative reconstruction result obtained with antenna #1 at a distance $d = 0$ m from the sample.

In particular, Figure 33 is the result with antenna #1, Figure 34 is the corresponding one with antenna #2, both in contact with the outer cylinder. The inner void inclusion was detected, located and correctly shaped in all these tomographic images. Its detected diameter corresponds to the actual value. An artifact appears near the center of the void PVC tube, and this is supposed to be due to the incorrect wave speed used for back-propagating the signals inside the void inclusion (propagation speed value in sand has been always used). As it happened in other cases, the better results are those obtained with antenna #1.

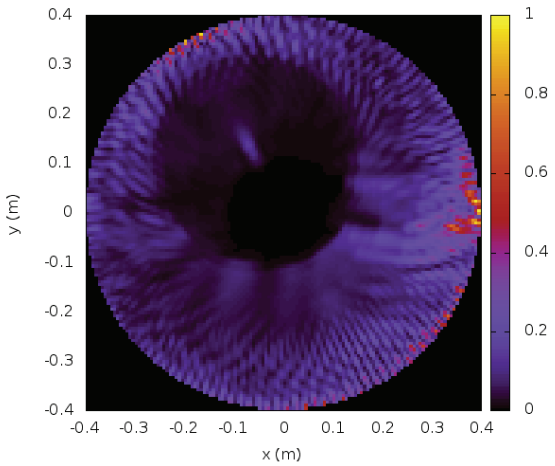

FIG. 34 – Circular cylinder with void inclusion. Qualitative reconstruction result obtained with antenna #2 at a distance $d = 0$ m from the sample.

4. FUTURE COLLABORATION WITH THE HOST INSTITUTION

The present STSM has been very useful not only to face the problem of the tomographical reconstruction of circular structures from an experimental point of view, but also for starting a cooperation between the University of Genoa and the Université Catholique de Louvain in the framework of the development and testing of new systems and reconstruction techniques applied to GPR measurements. This collaboration will be hopefully kept

active with the publication of joint works. Moreover, the processing and the inversion of the all data acquired during the present STSM is not yet completed, since it requires a significant effort from both a mathematical and a computational point of view. Therefore, the possibility of new scientific missions will be considered.

5. Foreseen publications/articles resulting from the STSM

The joint activities carried out during this STSM, expanded and integrated with further GPR data processing results that are currently in progress, are expected to be included in a scientific paper to be submitted to an IEEE peer-reviewed international journal, such as the IEEE Transactions on Geoscience and Remote Sensing.

6. Acknowledgements

The Authors thank COST, European Cooperation in Science and Technology, for funding COST Action TU1208 and this STSM.

7. References

[1] J. Je□ová, L. Mertens, and S. Lambot, "Ground-penetrating radar for observing tree trunks and other cylindrical objects," Constr. Build. Mater., vol. 123, pp. 214–225, Oct. 2016.

[2] M. Pastorino et al., "A microwave tomographic system for wood characterization in the forest products industry," Wood Mater. Sci. Eng., vol. 10, no. 1, pp. 75–85, 2015.

[3] A. Benedetto and L. Pajewski, Civil Engineering Applications of Ground Penetrating Radar. Cham: Springer International Publishing, 2015.

[4] I. Catapano, A. Randazzo, E. Slob, and R. Solimene, "GPR imaging via qualitative and quantitative approaches," in Civil Engineering Applications of Ground Penetrating Radar, A. Benedetto and L. Pajewski, Eds. Springer International Publishing, 2015, pp. 239–280.

[5] S. Lambot, E. C. Slob, I. van den Bosch, B. Stockbroeckx, and M. Vanclooster, "Modeling of ground-penetrating Radar for accurate characterization of subsurface electric properties," IEEE Trans. Geosci. Remote Sens., vol. 42, no. 11, pp. 2555–2568, Nov. 2004.

[6] A. Fedeli, M. Pastorino, and A. Randazzo, "A two-step multifrequency imaging technique for ground penetrating radar," in 2016 10th European Conference on Antennas and Propagation (EuCAP), 2016.

[7] C. Estatico, A. Fedeli, M. Pastorino, and A. Randazzo, "A multifrequency inexact-Newton method in Lp Banach spaces for buried objects detection," IEEE Trans. Antennas Propag., vol. 63, no. 9, pp. 4198–4204, Sep. 2015.

[8] M. Pastorino, Microwave imaging. John Wiley & Sons, 2010.

[9] S. Lambot and F. André, "Full-Wave Modeling of Near-Field Radar Data for Planar Layered Media Reconstruction," IEEE Trans. Geosci. Remote Sens., vol. 52, no. 5, pp. 2295–2303, May 2014.